IEICE TRANS. ELECTRON., VOL.E98–C, NO.12 DECEMBER 2015

PAPER

Dielectric Constant and Boundary Extraction Method for Double-Layered Dielectric Object for UWB Radars

Takuya NIIMI[†], **Shouhei KIDERA**[†a)], ***and*** **Tetsuo KIRIMOTO**[†], ***Members***

SUMMARY Microwave ultra-wideband (UWB) radar systems are advantageous for their high-range resolution and ability to penetrate dielectric objects. Internal imaging of dielectric objects by UWB radar is a promising nondestructive method of testing aging roads and bridges and a noninvasive technique for human body examination. For these applications, we have already developed an accurate internal imaging approach based on the range points migration (RPM) method, combined with a method that efficiently estimates the dielectric constant. Although this approach accurately extracts the internal boundary, it is applicable only to highly conductive targets immersed in homogeneous dielectric media. It is not suitable for multi-layered dielectric structures such as human tissues or concrete objects. To remedy this limitation, we here propose a novel dielectric constant and boundary extraction method for double-layered materials. This new approach, which simply extends the Envelope method to boundary extraction of the inner layer, is evaluated in finite difference time domain (FDTD)-based simulations and laboratory experiments, assuming a double-layered concrete cylinder. These tests demonstrate that our proposed method accurately and simultaneously estimates the dielectric constants of both media and the layer boundaries.

key words: *UWB radars, dielectric constant estimation, boundary extraction, non-destructive testing, range points migration (RPM) method, inverse scattering problem*

1. Introduction

There are emerging demands for innovative techniques that can image objects embedded in dielectric media. For instance, such techniques are potentially applicable to the noninvasive medical screening of human tissues and the monitoring of aging roads and bridges; the latter would reduce secondary damage in the event of a huge urban earthquake. Among the most promising technologies is the microwave ultra-wideband (UWB) radar system, which has the advantage of high-range resolution and the ability to penetrate dielectric objects. To realize the above applications, researchers have developed various internal imaging methods for targets buried in dielectric media, for example, the time-reversal [1] and space-time beamforming methods [2]. However, these methods are based on the waveform focusing approach, which assumes a pointwise target. Therefore, their accuracies and spatial resolutions are often insufficient for nonpointwise targets, and the computational burden becomes enormous in three-dimensional problems.

To solve the above problems, we previously proposed an accurate, high-speed UWB imaging method for targets buried in dielectric media [3]. However, this method assumes that the dielectric constant is given, which is an idealized situation. Moreover, the dielectric constant is used to convert the time delay to the actual target distance, so its value significantly affects the imaging accuracy. Various inverse scattering methods are available to reconstruct the real and imaginary components of the permittivity, such as numerical or analytical solutions of domain integral equations [4], [5]. However, such approaches need multidimensional optimization of the discretized region of interest (ROI), and the number of variable dimensions must be severely constrained to avoid sluggish convergence in the optimization process. Although other approaches reduce the computational burden by a geometric optics (GO) approximation [6], [7], they assume only a simple and known structure of the dielectric medium, such as a cuboid. Furthermore, they require accurate pre-estimation of the dielectric boundary and its normal vector.

Utilizing this background, we developed a promising method of simultaneously obtaining an accurate internal image and estimating the dielectric constant of the surrounding medium [8]. Prior to internal imaging, this method accurately reconstructs the dielectric boundary points and their normal vectors by the range points migration (RPM) [9] and Envelope interpolation methods [10]. The actual time delay of propagation through the dielectric medium is then accurately estimated from the recorded transmissive data. The waveform deformation, which degrades the imaging accuracy, is accurately compensated for by finite-difference time-domain (FDTD) data regeneration. However, this method is limited to a specific target model, namely, a highly conductive object (such as metal) buried in a single-layered homogeneous medium. For practical applications such as nondestructive inspection, inverse scattering of multilayered dielectric objects is desired. As a first step toward realizing such imaging, this paper extends our previous method [8] to imaging of double-layered dielectric medium. Our new method reconstructs the inner boundary points and their normal vectors by the extended envelope approach and directly estimates the dielectric constants of both layers by a GO-based propagation delay estimation. In numerical simulations and laboratory experiments, our proposed method simultaneously determined the dielectric constant and each boundary of a bi-layered dielectric object, without a priori information of the shape of each layer.

This paper comprises six sections. Section 2 describes

Manuscript received April 21, 2015.
Manuscript revised July 13, 2015.

[†]The authors are with Graduate School of Informatics and Engineering, The University of Electro-Communications, Chofu-shi, 182–8585 Japan.
a) E-mail: kidera@ee.uec.ac.jp

DOI: 10.1587/transele.E98.C.1134

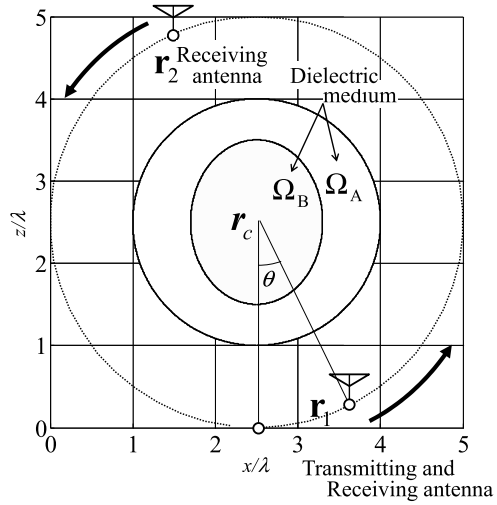

Fig. 1 System and observation model.

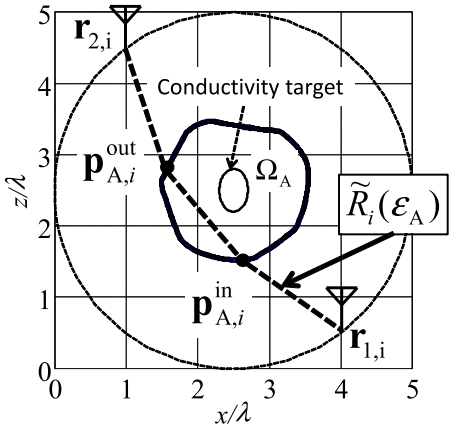

Fig. 2 Propagation path estimation in the conventional method.

our system and observation model, and Sect. 3 introduces the conventional method of estimating the dielectric constant [8]. Section 4 presents the principles of our proposed layer boundary and dielectric constant estimation. Section 5 evaluates the performance of the proposed method through numerical and experimental data, and a summary is presented in Sect. 6.

2. System and Observation Model

Figure 1 shows the system model. This paper deals with the two-dimensional problem, for simplicity. It is assumed that a dielectric object has a double layer structure. The regions for outer and inner medium are defined as Ω_A and Ω_B, respectively. Two omni-directional antennas are scanned along a circle with radius R_c centered at $\boldsymbol{r}_c$, which completely surrounds the dielectric object, as shown in Fig. 1. A set of transmitting and receiving antennas is located at $\boldsymbol{r}_1 = (X_1, Z_1)$, and an another receiving antenna is located at $\boldsymbol{r}_2 = (X_2, Z_2)$, and $\boldsymbol{r}_c = (\boldsymbol{r}_1 + \boldsymbol{r}_2)/2$ is fixed. The center wavelength of the transmitting signal is defined as λ. $S_1(X, Z, R)$ and $S_2(X, Z, R)$ are defined as the outputs of the Wiener filter at antenna positions $\boldsymbol{r}_1$ and $\boldsymbol{r}_2$, respectively, where $R = ct/2$ is expressed by time t and the propagation speed of radio wave c in air. The range points extracted from the local maxima of $S_1(X, Z, R)$ and $S_2(X, Z, R)$ are defined as $\boldsymbol{q}_1 = (X_1, Z_1, R_1)$ and $\boldsymbol{q}_2 = (X_2, Z_2, R_2)$, respectively, the extraction process is detailed in [8]. Each set including $\boldsymbol{q}_1$ and $\boldsymbol{q}_2$ is denoted Q_1 and Q_2, respectively.

3. Conventional Method

As a reference for the reader, this section briefly reports our former method [8]. Recall that this method accurately estimates the dielectric constant and extracts the boundary of highly conductive targets buried in homogeneous dielectric media. The dielectric boundary points and their normal vectors are reconstructed by sequential application of RPM [10] and envelope interpolation methods [10]. The dielectric object enclosing the target is assumed to have a single-layered structure. In this method, the set of range points $\boldsymbol{q}_{A,1}$, denoted as $Q_{A,1}$, is extracted from Q_1, where $S_1(\boldsymbol{q}_{A,1})$ has the maximum value at each antenna location (X, Z), regarded as the measured range from the antenna to the outer dielectric boundary. The outer dielectric boundary points are estimated and interpolated by sequentially applying the RPM and Envelope methods [10] to the range points $\boldsymbol{q}_{A,1}$. These boundary points are denoted as $\boldsymbol{p}_{A,j} = (x_{A,j}, z_{A,j})$ $(j = 1, \ldots N_A)$, where N_A is the total number of estimated outer boundary points. The set of all $\boldsymbol{p}_{A,j}$ is defined as $\partial\hat{\Omega}_A$. Next, the range points $\boldsymbol{q}_2$ included in Q_2 are used for the dielectric constant estimation by minimizing the difference between the estimated and observed propagation delays. The dielectric constant for the region Ω_A as ϵ_A is determined for each range point $\boldsymbol{q}_2$ as;

$$\hat{\epsilon}_{A,i} = \arg\min_{\epsilon_A} \left| R_{2,i} - \tilde{R}_i(\epsilon_A) \right|^2, \tag{1}$$

where $\tilde{R}_i(\epsilon_A)$ is calculated as;

$$\tilde{R}_i(\epsilon_A) = \left\| \boldsymbol{r}_{1,i} - \hat{\boldsymbol{p}}^{in}_{A,i} \right\| + \sqrt{\epsilon_A} \left\| \hat{\boldsymbol{p}}^{in}_{A,i} - \hat{\boldsymbol{p}}^{ex}_{A,i} \right\| + \left\| \hat{\boldsymbol{p}}^{ex}_{A,i} - \boldsymbol{r}_{2,i} \right\|. \tag{2}$$

Here, $\hat{\boldsymbol{p}}^{in}_{A,i}$ and $\hat{\boldsymbol{p}}^{ex}_{A,i}$ denote the incident and exit points on the dielectric boundary $\partial\hat{\Omega}_A$, determined by ensuring that the assumed dielectric constant ϵ_A and normal vectors on $\partial\hat{\Omega}_A$ satisfy Snell's law. Figure 2 shows an example of the propagation path estimation by this method.

Notably, the dielectric constant of the medium surrounding the embedded target is accurately estimated at considerably lower computational cost than that incurred by the domain integral equation [4], [5]. Furtheremore, unlike the methods typically used in through-the-wall applications [6], our method requires no *a priori* knowledge regarding the shape of the dielectric object. However, in principle, this method is applicable only to single-layered homogeneous media.

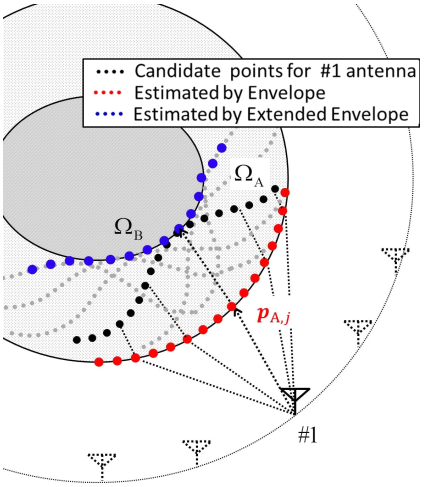

Fig. 3 Principle of extended Envelope method.

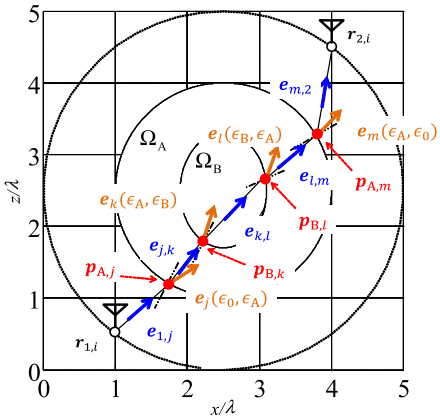

Fig. 4 Propagation path estimation in the proposed method.

4. Proposed Method

To alleviate the limitation mentioned in Sect. 3, this paper extends the former method [8] to a double-layered dielectric medium. Here, we introduce a new extended Envelope method that reconstructs the inner-layer boundary points and their normal vectors for the propagation path calculation. We also estimate the dielectric constants of both layers by a GO-based method. The methodology is detailed below.

4.1 Boundary Estimation by Extended Envelope Method

In this method, the outer dielectric boundary points are obtained by applying the Envelope method to the range points $\boldsymbol{q}_{A,1}$ as in Sect. 3, which is based on the non-parametric approach. These boundary points and their inclusion set are denoted $\boldsymbol{p}_{A,i}$, and $\partial\hat{\Omega}_A$, respectively. Second, the remaining range points are extracted from Q_1 as $\boldsymbol{q}_{B,1}$. The set of all $\boldsymbol{q}_{B,1}$, denoted as $Q_{B,1}$, should satisfy $Q_{B,1} = Q_1 \cap \overline{Q_{A,1}}$. To reconstruct the inner dielectric boundary $\partial\Omega_B$, the existing envelope method [10] is extended as follows. Figure 3 illustrates the reconstruction principle of the extended Envelope method. In this method, the candidate curve of the inner boundary point of each range point $\boldsymbol{q}_{B,1}$ is calculated by ensuring that the estimated outer dielectric boundary points $\boldsymbol{p}_{A,i}$ and their normal vectors satisfy Snell's law with the assumed ϵ_A. The outer envelope of the candidate curves is then extracted as the inner dielectric boundary $\partial\hat{\Omega}_B$. These inner boundary points are denoted as $\boldsymbol{p}_{B,j} = (x_{B,j}, z_{B,j})$ $(j = 1, \ldots, N_B)$. N_B is the total number of inner boundary estimation points. Since this method is based on the extended principle of Envelope, it also achieves a non-parametric estimation for inner boundary extraction.

4.2 Dielectric Constant Estimation by Transmissive Delay

We now explain the methodology for determining the dielectric constants in regions Ω_A and Ω_B. Similar to in Sect. 3, the dielectric constants are estimated by minimizing the observed and calculated transmissive delays. As a first step, the set of incident and exit points of each boundary for $\boldsymbol{q}_{2,i}$, $\left(\hat{\boldsymbol{p}}^{in}_{A,i}, \hat{\boldsymbol{p}}^{in}_{B,i}, \hat{\boldsymbol{p}}^{ex}_{B,i}, \hat{\boldsymbol{p}}^{ex}_{A,i}\right)$ on the dielectric boundary are determined by Snell's law as;

$$\begin{aligned}&\left(\hat{\boldsymbol{p}}^{in}_{A,i}, \hat{\boldsymbol{p}}^{in}_{B,i}, \hat{\boldsymbol{p}}^{ex}_{B,i}, \hat{\boldsymbol{p}}^{ex}_{A,i}\right)\\ &= \underset{(\boldsymbol{p}_{A,j},\boldsymbol{p}_{B,k},\boldsymbol{p}_{B,l},\boldsymbol{p}_{A,m}) \in \partial\hat{\Omega}_A{}^2\times\partial\hat{\Omega}_B{}^2}{\arg\min} \Big(\left\|\boldsymbol{e}_j(\epsilon_0,\epsilon_A) - \boldsymbol{e}_{j,k}\right\|^2\\ &\quad + \left\|\boldsymbol{e}_k(\epsilon_A,\epsilon_B) - \boldsymbol{e}_{k,l}\right\|^2 + \left\|\boldsymbol{e}_l(\epsilon_B,\epsilon_A) - \boldsymbol{e}_{l,m}\right\|^2\\ &\quad + \left\|\boldsymbol{e}_m(\epsilon_A,\epsilon_0) - \boldsymbol{e}_{m,2}\right\|^2\Big). \end{aligned} \tag{3}$$

Here, $\boldsymbol{e}_j(\epsilon_0,\epsilon_A) = \boldsymbol{R}^{rot}\left(\theta_j(\epsilon_0,\epsilon_A)\right)\left(-\boldsymbol{e}_{n,j}\right)$ holds, where $\boldsymbol{R}^{rot}$ denotes the 2-D rotation matrix, $\boldsymbol{e}_{n,j}$ is the normal unit vector on target point $\boldsymbol{p}_{A,j}$, and $\theta_j(\epsilon_0,\epsilon_A)$ is the refraction angle from the media with ϵ_0 to the media with ϵ_A determined by the Snell's law. $\boldsymbol{e}_k(\epsilon_A,\epsilon_B)$, $\boldsymbol{e}_l(\epsilon_B,\epsilon_A)$ and $\boldsymbol{e}_m(\epsilon_A,\epsilon_0)$ are similarly defined as the above. Also, $\boldsymbol{e}_{1,j}$, $\boldsymbol{e}_{j,k}$, $\boldsymbol{e}_{k,l}\boldsymbol{e}_{l,m}$ and $\boldsymbol{e}_{m,2}$ are defined as a unit vector between two target or antenna location points. Figure 4 plots the relationships among these vectors and points.

Next, for each range point $\boldsymbol{q}_{2,i}$, the propagation delay from $\boldsymbol{r}_{1,i}$ to $\boldsymbol{r}_{2,i}$ as $\tilde{R}_i(\epsilon_A,\epsilon_B)$ is calculated as follows:

$$\begin{aligned}\tilde{R}_i(\epsilon_A,\epsilon_B) &= \left\|\hat{\boldsymbol{p}}^{in}_{A,i} - \boldsymbol{r}_{1,i}\right\| + \sqrt{\epsilon_A}\left\|\hat{\boldsymbol{p}}^{ex}_{A,i} - \hat{\boldsymbol{p}}^{in}_{B,i}\right\|\\ &+ \sqrt{\epsilon_B}\left\|\hat{\boldsymbol{p}}^{in}_{B,i} - \hat{\boldsymbol{p}}^{ex}_{B,i}\right\| + \sqrt{\epsilon_A}\left\|\hat{\boldsymbol{p}}^{ex}_{B,i} - \hat{\boldsymbol{p}}^{ex}_{A,i}\right\|\\ &+ \left\|\hat{\boldsymbol{p}}^{ex}_{A,i} - \boldsymbol{r}_{2,i}\right\|. \end{aligned} \tag{4}$$

Figure 5 shows a representative propagation path and the incident and exit points on each boundary. The dielectric constants of the dielectric media for $\boldsymbol{q}_{2,i}$ are then determined as

$$(\hat{\epsilon}_{A,i}, \hat{\epsilon}_{B,i}) = \underset{(\epsilon_{A,i},\epsilon_{B,i})}{\arg\min}\left|R_{2,i} - \tilde{R}_i(\epsilon_A,\epsilon_B)\right|^2. \tag{5}$$

Finally, for all transmissive range points $\boldsymbol{q}_2$, the dielectric constants are optimized by

$$(\hat{\epsilon}_A, \hat{\epsilon}_B) = \frac{\sum_{i=1}^{N_2} S_2(\boldsymbol{q}_{2,i})(\hat{\epsilon}_{A,i}, \hat{\epsilon}_{B,i})}{\sum_{i=1}^{N_2} S_2(\boldsymbol{q}_{2,i})}, \tag{6}$$

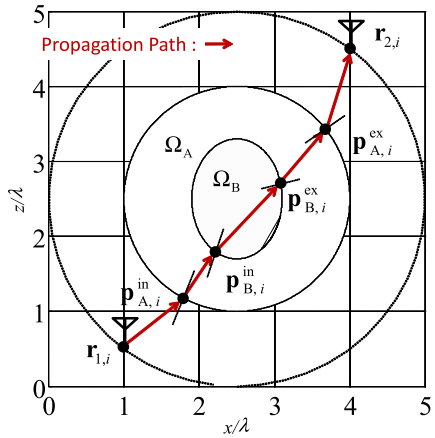

Fig. 5 Propagation path estimation in the proposed method.

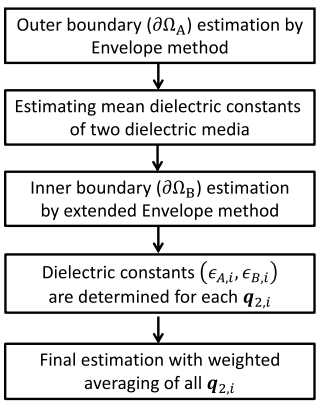

Fig. 6 Flowchart of the proposed method.

where N_2 is the total number of range points $\boldsymbol{q}_2$.

4.3 Procedure of Proposed Method

The procedure of the method is summarized below.

Step 1) One set of range points $Q_{\mathrm{A},1}$ with components $\boldsymbol{q}_{\mathrm{A}}$ is extracted from Q_1, where $S_1(\boldsymbol{q}_{\mathrm{A}})$ has the maximum value at each antenna location. The other set of range points $Q_{\mathrm{B},1}$ with components $\boldsymbol{q}_{\mathrm{B}}$ is extracted, where $Q_{\mathrm{B},1} = Q_1 \cap \overline{Q_{\mathrm{A},1}}$ satisfies.

Step 2) Outer boundary is estimated as $\partial\hat{\Omega}_{\mathrm{A}}$ by applying the Envelope method to $Q_{\mathrm{A},1}$.

Step 3) Initial dielectric constants for both media are determined as ϵ_{init} by applying the method in [8] (which assumes a single layered medium) to $\boldsymbol{q}_2$.

Step 4) For each range point $\boldsymbol{q}_{2,i}$, both dielectric constants as $(\hat{\epsilon}_{\mathrm{A},i}, \hat{\epsilon}_{\mathrm{B},i})$ are estimated as in Eq. (5), where the internal layer boundary points as $\partial\hat{\Omega}_{\mathrm{B}}$ are sequentially updated by applying the extended Envelope method to $Q_{\mathrm{B},1}$. with the assumed ϵ_{A}.

Step 5) Optimal dielectric constants as $(\hat{\epsilon}_{\mathrm{A}}, \hat{\epsilon}_{\mathrm{B}})$ are computed by Eq. (6), using all range points $\boldsymbol{q}_{2,i}$ in Q_2.

Figure 6 shows the flowchart of the proposed method.

5. Performance Evaluation

This section investigates the performance evaluation of the proposed method with the numerical simulation by FDTD (Finite-Difference Time-Domain) analysis and the experiment, assuming double-layered concrete as the target material.

5.1 Evaluation in Numerical Simulation

In the numerical simulation, as described in Sect. 2, the two antennas located as $\boldsymbol{r}_1$ and $\boldsymbol{r}_2$ are simultaneously scanned around the circumference of a circle with radius 2.5λ and center $\boldsymbol{r}_{\mathrm{c}} = (2.5\lambda, 2.5\lambda)$. 50 equally spaced data points are observed across the range $0 \le \theta \le 2\pi$. Each signal received on $\boldsymbol{r}_1$ and $\boldsymbol{r}_2$ is generated by FDTD, assuming the TE mode wave. In the FDTD simulation, the induced current waveform at the transmitting antenna forms a mono-cycle pulse defined as;

$$i(t) = \begin{cases} \left(1 - \cos\frac{2\pi t}{T}\right)\sin\frac{2\pi t}{T} & (0 < t \le T) \\ 0 & (\text{otherwise}) \end{cases}, \tag{7}$$

where $T = \lambda/\mathrm{c}$. The time step interval for the FDTD calculation is set to $T/200$, and each spatial cell size along the x and z axes is $\lambda/80$. The analysis range is $0 \le x, z \le 5\lambda$, where the Mur second-order absorbing boundary is employed.

We first simulate a simple case (called Case #1), assuming the dielectric object as shown in Fig. 1, in which each outer boundary of Ω_{A} and Ω_{B} forms circular and ellipsoidal boundary, respectively. Assuming typical parameters of concrete, the dielectric constants of the outer and inner dielectric media are set to $\epsilon_{\mathrm{A}} = 5.0$ and $\epsilon_{\mathrm{B}} = 3.0$, respectively, and the conductivity of each medium is set to 0.01 S/m. A noiseless situation is assumed. The upper and lower panels of Fig. 7 show the outputs of the Wiener filter $S_1(X, Z, R)$ and $S_2(X, Z, R)$, respectively and the corresponding range points in Case #1, where the horizontal axis θ denotes $\theta = \tan^{-1}\left(\frac{X - X_{\mathrm{C}}}{Z - Z_{\mathrm{C}}}\right)$ (see Fig. 1). As shown in the upper panel of Fig. 7, the range points reflected from the outer and inner boundaries ($\boldsymbol{q}_{\mathrm{A},1}$ and $\boldsymbol{q}_{\mathrm{B},1}$, respectively) are clearly separated. The dielectric constants estimated from Eq. (6) are $\hat{\epsilon}_{\mathrm{A}} = 5.29$ (relative error of 6%) and $\hat{\epsilon}_{\mathrm{B}} = 2.95$ (relative error of 2%). Figure 8 shows the dielectric boundary reconstructed by the Envelope and the extended Envelope methods using the estimated dielectric constants of both media. According to this figure, our method can accurately estimate both boundaries without *a priori* knowledge of of the dielectric constants. The obtained images are quantitatively evaluated by the root-mean-square error (RMSE) of each boundary, computed as

$$\mathrm{RMSE} = \sqrt{\frac{1}{N}\sum_{j=1}^{N_{\mathrm{tar}}} \min_{\boldsymbol{r}_{\mathrm{true}}} \left|\boldsymbol{r}_j - \boldsymbol{r}_{\mathrm{true}}\right|^2}, \tag{8}$$

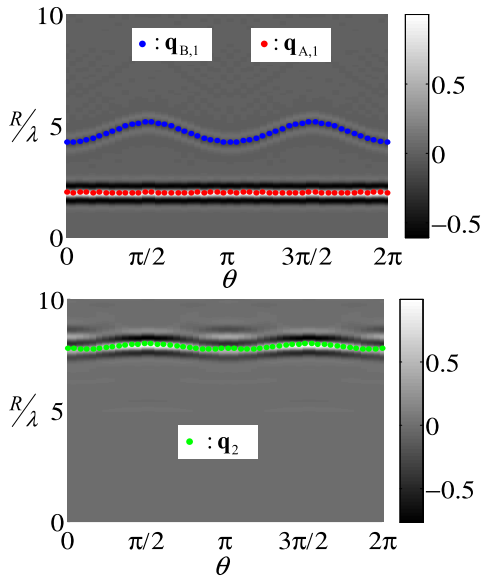

Fig. 7 Outputs of Wiener filter $S_1(X,Z,R)$ (upper) and $S_2(X,Z,R)$ (lower) in Case #1.

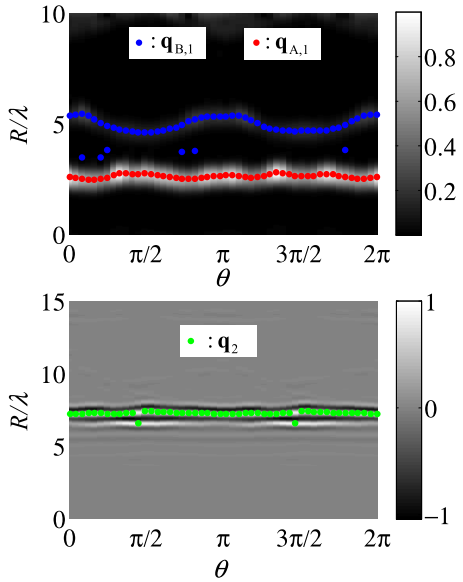

Fig. 9 Outputs of Wiener filter $S_1(X,Z,R)$ (upper) and $S_2(X,Z,R)$ (lower) in Case #2.

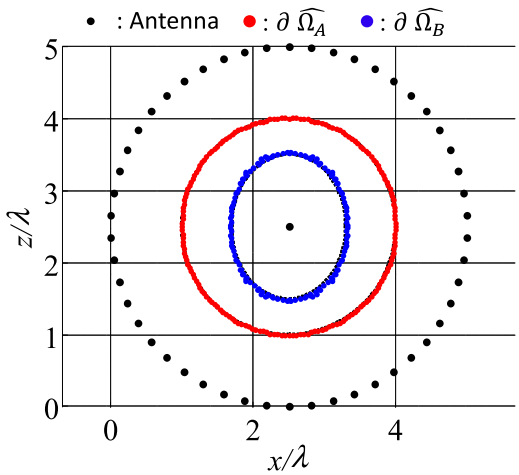

Fig. 8 Estimated dielectric boundaries for Ω_A and Ω_B using the proposed method in Case #1.

where $\boldsymbol{r}_{\text{true}}$ and $\boldsymbol{r}_j$ denote the actual and estimated boundary points in each layer, respectively, and N_{tar} is the total number of estimated boundary points along each boundary. In the Case #1, the RMSEs for $\partial\Omega_A$ and $\partial\Omega_B$ are $6.2\times10^{-3}\lambda$ and $2.9\times10^{-2}\lambda$, respectively. This highly accurate boundary extraction is essentially derived from the accurate estimation of dielectric constants in the double-layered media.

Next, to investigate more general dielectric boundary case, the Case #2 is assessed, where the outer dielectric boundary is not expressed as an analytical function, but is generated by giving white Gaussian values along the radial direction from the origin $(2.5\lambda, 2.5\lambda)$ with mean value 1λ, and standard deviation 1λ. Then, these fluctuations on the outer boundary are spatially smoothed by a Gaussian function with a correlation length of 0.2λ. In this case, the dielectric constants of the outer and inner dielectric media are set to $\epsilon_A = 3.0$ and $\epsilon_B = 6.0$, respectively, The upper and lower sides of Fig. 9 show the outputs of the Wiener filter as $S_1(X,Z,R)$ and $S_2(X,Z,R)$, respectively, in Case #2. Especially in the reflection signals (upper panel), there are some unnecessary range points in $\boldsymbol{q}_{B,1}$ that precede the desired range points. These undesirable signals are caused by a side-lobe echo effect from the boundary of $\partial\Omega_A$, because they appear when $\boldsymbol{q}_{A,1}$ and $\boldsymbol{q}_{B,1}$ approach each other. The dielectric constants estimated from Eq. (6) are $\hat{\epsilon}_A = 3.21$ (relative error of 10%) and $\hat{\epsilon}_B = 6.62$ (relative error of 11%). Figure 10 shows the dielectric boundary reconstructed by the Envelope and extended Envelope methods, using the estimated dielectric constants of both media. The lower panel enlarges the region enclosed by the blue boundary in the upper panel. This figure reveals that, although the envelope method accurately expresses the outer boundary $\partial\Omega_A$, the extended version does not precisely estimate the inner boundary $\partial\Omega_B$. This can be explained by the fact that an antenna $\boldsymbol{r}_1$ cannot receive a strong echo from the inner boundary area, which is not accurately reconstructed, due to the path skewed by the concave part of the outer boundary. In the Case #2, the RMSEs of the outer and inner boundary are $1.1\times10^{-2}\lambda$ and $3.4\times10^{-2}\lambda$, respectively. It should be noted that the processes for each dielectric constant estimation collectively require approximately 12 hours of calculation time, while each outer and inner boundary estimation by Envelope method is just within 2 second, respectively, with Xeon 2.8GHz Processor. This is because at each range point, we search for two dielectric constants; namely, we assess all discretized 2-dimensional points (ϵ_A, ϵ_B) within a certain range ($1.0 \le \epsilon \le 10.0$ in this case) with small spacing ($\Delta\epsilon = 0.1$ in this case) to avoid trapping in a local minimum. The calculation cost can be reduced by optimizing the source code (MATLAB in this case), or integrating our

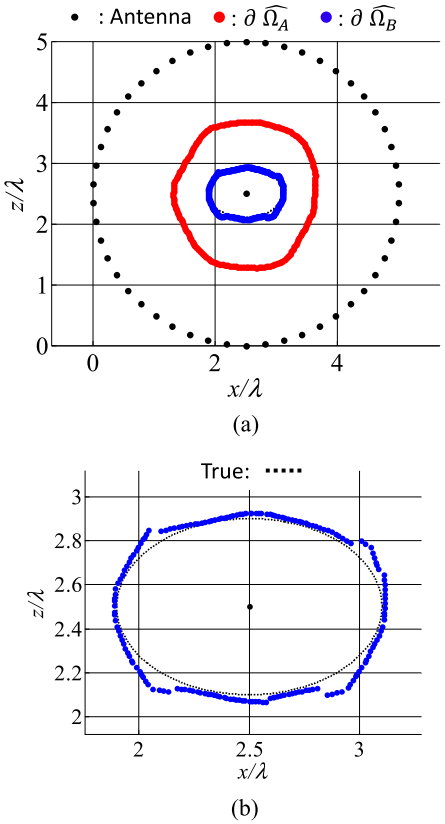

Fig. 10 (a) Estimated dielectric boundaries for Ω_A and Ω_B using the proposed method, (b): Enlarged view for Ω_B in Case #2.

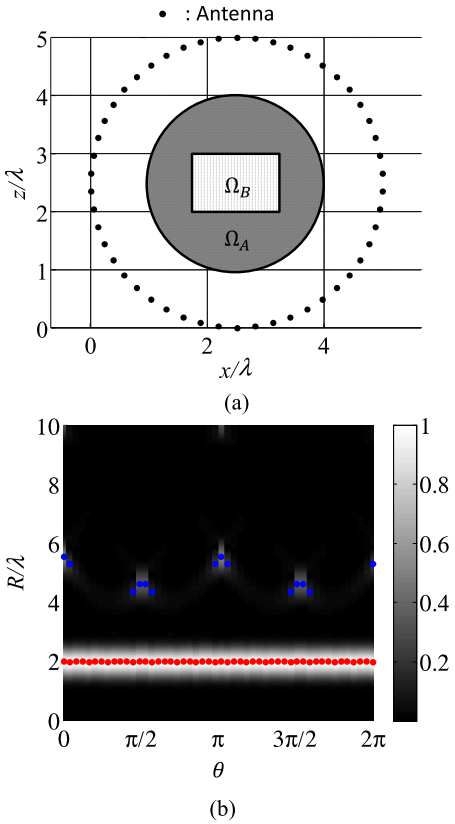

Fig. 11 (a) Actual boundary assuming the rectangular inner object, (b): Output of Wiener filter $S_1(X, Z, R)$.

method with a more efficient optimization algorithm, such as the Levenberg-Marquardt method.

Furthermore, we should mention the application range of this method, particular with respect to the shape of the inner boundary. In the aforementioned cases, we can reconstruct the entire shape of the inner boundary, because a reflection echo from each scattering point on the inner boundary is detectable of $S_1(X, Z, R)$ in our assumed observation geometry. However, if this is not the case, our method is substantially inapplicable, because the propagation path cannot be correctly estimated from a partial shape of the inner boundary. As an example, Fig. 11 shows an inner rectangular shape embedded in a circular outer boundary, where $\epsilon_A = 3.0$ and $\epsilon_B = 6.0$ are set. As shown in the lower side of Fig. 11, the number of reflection range points obtained from the inner boundary is insufficient for correctly extracting the inner boundary; thus, the dielectric constant cannot be properly estimated by the proposed method. This problem might be resolved by extending the multi-static configuration, which expands the reconstruction area of the inner boundary [11]. Such an extension will be attempted in our future work.

5.2 Evaluation with Experimental Data

In this subsection, the proposed method is evaluated in an experiment configured in an anechoic chamber. The experimental setup is illustrated in Fig. 12. The antenna is a cross-dipole antenna in vertical polarization mode. The single transmitting antenna is located at $\boldsymbol{r}_T$, and the signal data $S_1(X, Z, R)$ and $S_2(X, Z, R)$ are observed at the two receiving antennas $\boldsymbol{r}_{R1}$ and $\boldsymbol{r}_{R2}$, respectively. To accomplish the circular scanning model described in Sect. 2, the dielectric object is rotated about the center $\boldsymbol{r}_C$, fixing the location of the antennas $\boldsymbol{r}_T$, $\boldsymbol{r}_{R1}$ and $\boldsymbol{r}_{R2}$. To guarantee a sufficient accuracy for target manufacturing at the order of 1/100 transmitting wavelength (around 1 mm), this experiment assumes a simple shape case. Specifically, a cylindrical mortal mix Ω_B is buried in the cylindrical cement Ω_A, and both cylinders are 300mm high. The radii of the mortal and cement mediums are 298 mm and 195 mm, respectively. The actual dielectric constants of the dielectric object (cement and mortal) were measured by averaging the propagation delays

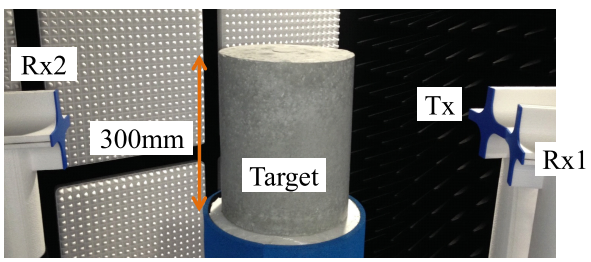

Fig. 12 Experimental setup.

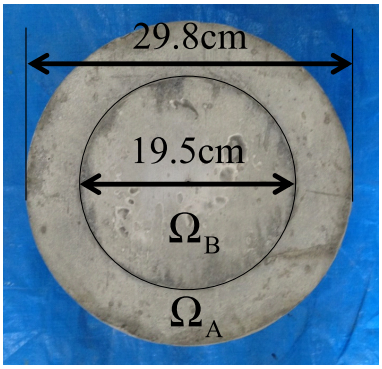

Fig. 13 Concrete target with double-layered structure.

observed from 50 different angles, assuming a cylindrical dielectric object fabricated from each material. In this way, the dielectric constants of the cement and mortal objects are measured as approximately 10.9 and 9.7, respectively, which are regarded as the actual values in this experiment. The target rotation center is set to $\boldsymbol{r}_C = (400\text{mm}, 400\text{mm})$, and the distance from the antenna, namely, R_C is set to 400 mm. The received signal is obtained using a VNA (Vector Network Analyzer), where the frequency is swept from 1000 MHz to 3000 MHz at 10 MHz intervals. S_1, S_2 are obtained by applying the inverse discrete Fourier transform to the acquired frequency data. The effective bandwidth is around 2.0 GHz, corresponding to a range resolution of approximately 75 mm. The center frequency is also 2.0 GHz (center wavelength: 150 mm).

Here, the average S/Ns of $S_1(X,Z,R)$ and $S_2(X,Z,R)$ are 42 dB, 34 dB, respectively, where the S/N is defined as the ratio of the peak instantaneous signal power to average noise power after applying a matched filter. In addition, to suppress the range sidelobe caused by relatively narrower fractional bandwidth of the transmitted signal compared with that assumed in numerical simulation, the Capon filter is used for range point extraction, which is detailed in [12]. The upper and lower sides of Fig. 14 show the outputs of the Capon filter as $S_1^{\mathrm{CP}}(X,Z,R)$ and $S_2^{\mathrm{CP}}(X,Z,R)$ in the experimental case, respectively, after the direct signal elimination. Here, since the contrast between ϵ_A and ϵ_B is considerably smaller than that assumed in the previous numerical simulations, each antenna receives significantly smaller reflection echoes from the inner boundary, thus increasing the relative error in the range extraction. To confirm this fact, Fig. 15 shows a shapshot of $S_1(X,Z,R)$ and $S_1^{\mathrm{CP}}(X,Z,R)$. In this figure, while the range sidelobe caused by the reflection echo from the 1st layer can be suppressed by the Capon method compared with that obtained by the Wiener filter, the reflection amplitude from the 2nd layer is considerably lower because of the low contrast of the dielectric constants. Note the undesirable signals around $R = 0.9$ m in the $S_2^{\mathrm{CP}}(X,Z,R)$ output. These are attributed to a creeping wave propagating along the dielectric outer boundary. We previously developed a method that suppresses creeping signals without *a priori* knowledge of the outer dielectric

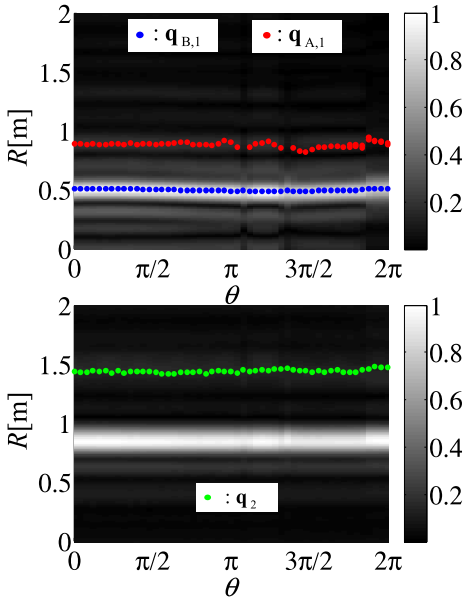

Fig. 14 Outputs of Capon method as $S_1^{\mathrm{CP}}(X,Z,R)$ (upper) and $S_2^{\mathrm{CP}}(X,Z,R)$ (lower) and the extracted range points in the experiment.

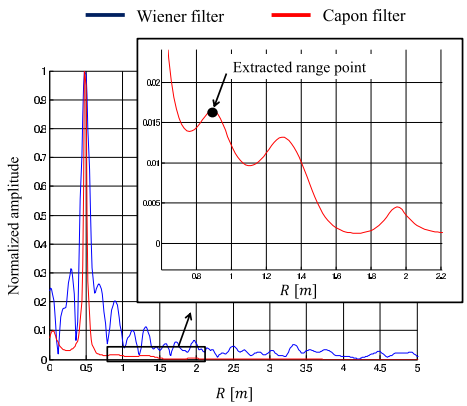

Fig. 15 Snapshot of output of Wiener filter and Capon method in the experiment at $\theta = 0$.

boundary [13]. Applying this method to $S_2^{\mathrm{CP}}(X,Z,R)$, we obtained the actual transmissive delays (plotted as the range points $\boldsymbol{q}_2$ in the bottom panel of Fig. 14).

In this case, the estimated dielectric constants using Eq. (6) in the proposed method, are $\hat{\epsilon}_A = 10.68$ (relative error of 2.5%) and $\hat{\epsilon}_B = 9.02$ (relative error of 7%), respectively. It should be noted that these accuracies are accomplished based on *a priori* knowledge of two-layered dielectric medium assumptions, and considerably high SNR data that is required for applying the Capon method. Figure 16 shows each reconstructed image of the double layered dielectric media, as $\partial\hat{\Omega}_A$ and $\partial\hat{\Omega}_B$, respectively, where the estimated dielectric constants are used for the extended Envelope method. Note that, since the bi-static radar model is used in this experiment, the both boundary estimated methods, as the Envelope and the extended Envelope methods, are modified to this observation model. The RMSEs of the

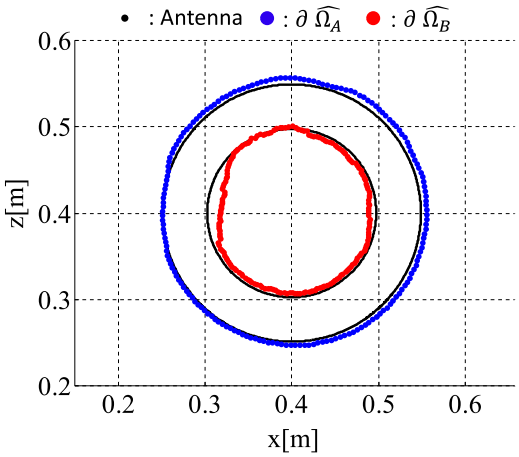

Fig. 16 Estimated dielectric boundaries for Ω_A and Ω_B using the proposed method in the experiment.

outer and inner boundary are about 6.5 mm ($4.3 \times 10^{-2}\lambda$) and 7.7 mm ($5.1 \times 10^{-2}\lambda$), respectively. This result confirms that our proposed method enables highly accurate boundary extraction in realistic scenarios; indeed, the accuracy is on the order of 1/100 of the transmitting wavelength, which is sufficient for practical applications. However, as shown in Fig. 16, part of the estimated inner boundary $\partial\Omega_B$ is rendered inaccurate by errors in the range points. These inaccuracies are caused by side lobe effects or clutters that cannot be eliminated by the Capon method, and by the considerably smaller contrast between ϵ_A and ϵ_B than that assumed in the numerical simulation. Because the accuracy and resolution of the range point extraction directly affects the accuracy of the dielectric constant and boundary estimates, the accuracy or resolution of the range points should be improved by adopting super-resolution techniques.

6. Conclusion

This paper proposed a method of accurately estimating the dielectric constants and boundary shapes of double-layered dielectric objects. Notably, the method is applicable to arbitrary target shapes and enables accurate estimation of both dielectric constants and boundaries without *a priori* knowledge of the boundary shapes. It also exploits a unique characteristic of the newly developed extended envelope method, enabling accurate estimation not only of the points along the inner boundary but also of their normal vectors. Using this feature and Snell's law, we can determine the possible propagation path into a double-layered dielectric medium. In both numerical and experimental trials, our proposed method accurately estimated the dielectric constants and thereby extracted the boundaries to accuracy on the order of 1/100 of the transmitting center wavelength. As a final remark, although the present study was restricted to double-layered media, the proposed approach is easily extendable to multi-layered materials, provided that the number of layers is known beforehand. Our proposed method will be evaluated on multi-layered dielectric objects in our future work.

Acknowledgments

This work was supported by Grant-in-Aid for Young Scientists (A) by JSPS KAKENHI Grant Number 26709030, the SCOPE (Grant No. 132103001) promoted by Japanese Ministry of Internal Affairs and Communications, Japan, the Research Grant (Basic Research) promoted by TEPCO Memorial Foundation, the Nakajima Foundation, the Kurata Memorial Hitachi Science and Technology Foundation, the Tateishi Science and Technology Foundation and the Yazaki Memorial Foundation for Science and Technology and the Ozawa-Yoshikawa Memorial Electronics Foundation.

References

[1] P. Kosmas and C.M. Rappaport, "A Matched-Filter FDTD-Based Time Reversal Approach for Microwave Breast Cancer Detection," IEEE Trans. Antennas Propagat., vol.54, no.4, pp.1257–1264, April 2006.
[2] X. Li, E.J. Bond, B.D. Van Veen, and S.C. Hagness, "An overview of Ultra-Wideband Microwave Imaging via Space-Time Beamforming for Early-Stage Breast-Cancer Detection," IEEE Antennas Propagat. Mag., vol.47, no.1, pp.19–34, Feb. 2005.
[3] K. Akune, S. Kidera, and T. Kirimoto, "Accurate and Nonparametric Imaging Algorithm for Targets Buried in Dielectric Medium for UWB Radars," IEICE Trans. Electronics, vol.E95-C, no.8, pp.1389–1398, Aug. 2012.
[4] A. Franchois and C. Pichot, "Microwave Imaging-Complex Permittivity Reconstruction with a Levenberg-Marquardt Method," IEEE Trans. Antennas Propagat., vol.45, no.2, pp.203–215, Feb. 1997.
[5] R. Autieri, M. Urso, T. Isernia, and V. Pascazio, "Inverse Profiling via an Effective Linearized Scattering Model and MRF Regularization," IEEE Trans. Geosci. & Remote Sens., vol.8, no.6, pp.1021–1025, Nov. 2011.
[6] P. Protiva, J. Mrkvica, and J. Machac, "Estimation of Wall Parameters From Time-Delay-Only Through-Wall Radar Measurements," IEEE Trans. Antennas Propagat., vol.59, no.11, pp.4268–4278, Nov. 2011.
[7] R. Solimene, R.D. Napoli, F. Soldovieri, and R. Pierri, "TWI for an Unknown Symmetric Lossless Wall," IEEE Trans. Geosci. & Remote Sens., vol.49, no.8, pp.2876–2886, Aug. 2011.
[8] R. Souma, S. Kidera, and T. Kirimoto, "Accurate Permittivity Estimation Method with Iterative Waveform Correction for UWB Internal Imaging Radar" IEICE Trans. Electronics, vol.E96-C, no.5, pp.730–737, May 2013.
[9] S. Kidera, T. Sakamoto, and T. Sato, "Accurate UWB Radar Three-Dimensional Imaging Algorithm for a Complex Boundary Without Range Point Connections," IEEE Trans. Geosci. Remote Sens., vol.48, no.4, pp.1993–2004, April 2010.
[10] S. Kidera, T. Sakamoto, and T. Sato, "A Robust and Fast Imaging Algorithm with an Envelope of Circles for UWB Pulse Radars," IEICE Trans. Commun., vol.E90-B, no.7, pp.1801–1809, April 2007.
[11] Y. Niwa, S. Kidera, and T. Kirimoto, "Image Expansion Approach for Target Buried in Dielectric Medium with Extended RPM to Multi-static UWB Radar," IEICE Trans. Electronics, vol.E96-C, no.1, pp.119–123, Jan. 2013.
[12] S. Kidera, T. Sakamoto, and T. Sato, "Super-Resolution UWB Radar Imaging Algorithm Based on Extended Capon with Reference Signal Optimization," IEEE Trans. Antennas. & Propagation., vol.59, no.5, pp.1606–1615, May 2011.
[13] T. Manaka, S. Kidera, and T. Kirimoto, "Experimental Study on Permittivity Estimation Method for UWB Internal Imaging

Radar," 2014 International Symposium on Antennas and Propagation (ISAP2014), pp.153–154, Dec. 2014.

Takuya Niimi received his B.E. degree in Electronic Engineering from University of Electro-Communications in 2013 and M.E degree at the Graduate School of Informatics and Engineering, University of Electro-Communications in 2015.

Shouhei Kidera received his B.E. degree in Electrical and Electronic Engineering from Kyoto University in 2003 and M.I. and Ph.D. degrees in Informatics from Kyoto University in 2005 and 2007, respectively. He is currently an Associate Professor in Graduate School of Informatics and Engineering, the University of Electro-Communications, Japan. His current research interest is in advanced radar signal processing or electromagnetic inverse scattering issue for ultra wideband (UWB) sensor. He was awarded Ando Incentive Prize fo the Study of Electronics in 2012, Young Scientist's Prize in 2013 by the Japanese Minister of Education, Culture, Sports, Science and Technology (MEXT), and Funai Achievement Award in 2014. He is a member of the Institute of Electrical and Electronics Engineering (IEEE) and the Institute of Electrical Engineering of Japan (IEEJ).

Tetsuo Kirimoto received the B.S. and M.S. and Ph.D degrees in Communication Engineering from Osaka University in 1976, 1978 and 1995, respectively. During 1978–2003 he stayed in Mitsubishi Electric Corp. to study radar signal processing. From 1982 to 1983, he stayed as a visiting scientist at the Remote Sensing Laboratory of the University of Kansas. From 2003 to 2007, he joined the University of Kitakyushu as a Professor. Since 2007, he has been with the University of Electro-Communications, where he is a Professor at the Graduate School of Informatics and Engineering. His current study interests include digital signal processing and its application to various sensor systems. Prof. Kirimoto is a senior member of IEEE and a member of SICE (The Society of Instrument and Control Engineers) of Japan.